
The Double Pendulum: An Experimental Design Report

A PREPRINT

Audun D. Myers

Department of Mechanical Engineering
Michigan State University
East Lansing, MI
myersau3@msu.edu

Firas A. Khasawneh

Department of Mechanical Engineering
Michigan State University
East Lansing, MI
khasawn3@egr.msu.edu

Joshua R. Tempelman

Department of Mechanical Engineering
Michigan State University
East Lansing, MI
tempelm2@msu.edu

David Petrushenko

Department of Mechanical Engineering
Virginia Tech.
Blacksburg, VA
petrusd26@cvt.edu

March 23, 2020

Abstract

The double pendulum is a relatively simple bench top experiment that exhibits complex dynamics. This makes it a very useful for experimentally validating dynamic systems analysis tool. In this report, the manufacturing, design, and parameter identification of a double pendulum is discussed in detail. Specific equipment and mechanical drawings are provided to allow the reader to replicate the experiment and results found. Additionally, a new tracking algorithm based on the nearest neighbors algorithm is introduced for tracking the position of both links of the double pendulum.

Contents

1	Introduction	2
2	Equipment	3
3	Manufacturing and Assembly Process	3
3.1	Double Pendulum Assembly	4
3.2	Marker Design and Assembly	4
4	Equations of Motion	5
4.1	Component Energy Equations	5
4.2	Equations of motion	8
5	Data Collection and Analysis	9

5.1	Encoder Data Collection and Calibration	9
5.2	Video Data Collection and Calibration	9
5.2.1	Pendulum Error Analysis for Video Data	10
5.2.2	Pendulum Measurements Using Video Data	11
6	Data Validation	12
6.1	Damping Parameter Estimation	12
A	Additional Information	17
A.1	Bearing Kinematics: Velocity Analysis using Absolute velocities	17
A.2	Velocity Analysis using a frame attached to $\overline{OC_0}$	18
A.3	Uncertainty in the Bearing Ball Locations	19
A.4	Multiple Object Tracking with Occlusions Algorithm	19
A.4.1	Pendulum Error Analysis Details	20
A.5	Double pendulum component measurements	21
A.6	Mechanical Drawings	23

1 Introduction

The double pendulum has been studied both experimentally [2, 3, 4, 5] and numerically [1, 6]. However, a thorough process for manufacturing and collecting data from a double pendulum has not yet been completed. In this work, we provide a step-by-step guide to any researcher hoping to establish a pipeline to fabricate such a device, make accurate measurements the systems dynamics, and validate the empirical data with numerical models.

This paper is organized as follows. The equipment and material lists provided for a bench top double pendulum in Sections 2 and 3. The detailed equations of motion for the experimental setup are developed in Section 4. The data collection and analysis methods are then discussed in Section 5, which are shown to provide accurate measurements. Following the data collection section, the method we used to simulate the pendulum is discussed in Section 6. Section 6.1 discusses the damping models for the pendulum links and bearings are stated and parameters for these models are estimated through an energy dissipation approach.



Figure 1: CAD rendering of bench top double pendulum.

2 Equipment

The experimental equipment used in the double pendulum are separated into three categories: (1) video equipment for tracking (see Table 1), (2) equipment used to assemble double pendulum (see Table 2), and (3) manufactured components (see Table 3). For Table 3, mechanical drawings for each component are provided in Section A.6. Additionally, a reference to all the moving components is provided in Fig. 6

Table 1: Equipment used for tracking both links of double pendulum.

Item No.	Description	Item Name	Manufacturer	S/N
1	High Speed Camera	FASTCAM Mini UX50	Photron	10445045947
2	Personal Computer	OptiPlex 7050	Dell	C2J7XM2
3	High Speed Lighting Kit	Varsa V2	Nila	V0002201
4	Absolute Rotary Encoder	UCD-AC005-0413-R06A-CRW	Posital	2532295
5	Data Acquisition System	NI USB-6356	National Instruments	1C91A61
6	DC Power Supply	Model 1761	BK Precision	214F16175
7	BNC cables	Unknown	Unknown	NA
8	Camera Lens	AF Zoom-NIKKOR 24-85mm	Nikon	NA
9	Pendulum Stand Clamp	340-RC	Newport	NA
10	Pendulum Stand Post	40	Newport	NA
11	Pendulum Stand Base	300-P	Newport	NA
12	Non-reflective Tape	Black Masking Tape	ProTapes	NA
13	Reflective Tape	Unknown	Unknown	NA
14	Backdrop	Black Background Backdrop	Issuntex	NA
15	Camera Stand	Unknown	Unknown	Unknown

Table 2: Equipment used for assembling manufactured double pendulum components.

Item No.	Description	Quantity	Item Name	Manufacturer	SKU or UPC
1	Encoder Flange	2	Bones Swiss Bearings	Bones Swiss	BSAWBX8S
2	8mm x 6mm Flexible coupling	1	Flexible Shaft Coupling	McMaster	2463K6
3	M3 x 0.5 x 8	4	M3 bolt	McMaster	92855A309
4	8-32 UNC x 0.5	4	8-32 bolt	McMaster	91772A194
5	1/4-20 UNC x 1.5	4	1/4"-20 bolt	McMaster	92196A706
6	8-32 Threaded Insert	4	Threaded insert	McMaster	92394A114
7	M8 x 24mm hollow dowel pin	1	Hollow dowel pin	McMaster	97184A260

Table 3: Manufactured components for of double pendulum. Mechanical drawings for each manufactured component are provided in Section A.6.

Item No.	Description	Quantity	Material	Dwg. No. (Section A.6)
1	Encoder Flange	1	3D printed ABS	Dwg No. 1
2	Encoder Mount	1	3D printed ABS	Dwg No. 2
3	Circular Tracker	1	3D printed PLA	Dwg No. 3
4	Upper Link	1	6061 Aluminum	Dwg No. 4
5	Side Tracker	1	3D printed PLA	Dwg No. 5
6	Lower Link	1	6061 Aluminum	Dwg No. 6

3 Manufacturing and Assembly Process

There are two main stages to assembling the double pendulum. The first is to attach the encoder to the upper joint of the upper link, which is detailed in Fig. 2. Specifically, the encoder axis is connected to the

upper axis of rotation through the flexible coupling. The encoder and shaft are held in position by a 3D printed mount and flange. Additionally, the shaft is pressure fit into the upper links to prevent slipping.

3.1 Double Pendulum Assembly

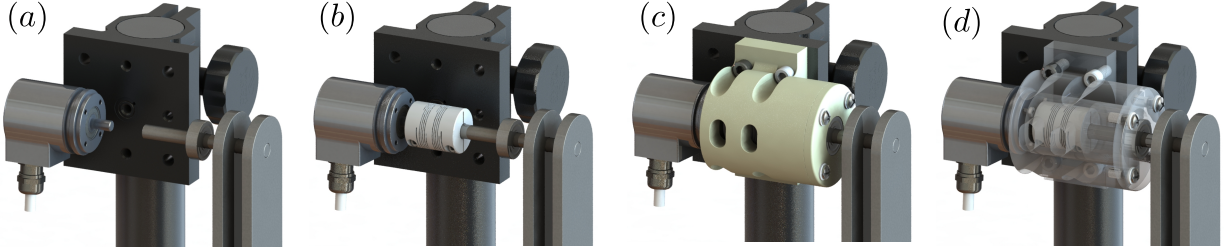


Figure 2: Assembly process for upper joint. (a) axis of encoder and upper joint aligned, (b) flexible coupling attached to upper shaft and encoder, (c) flange and mounting attached to secure encoder and upper shaft, (d) transparent mounting provided to show bolt layout.

The second stage of assembly is to configure the lower joint. This is done by first pressure fitting the hollow dowel pin into the lower bearing. The lower bearing is then pressure fit into the lower link. Next, the outside of the hollow dowel pin is pressure fit into both of the upper links. A second down pin can be housed in the hollow dowel. This second pin can be inserted through the small hole on the top of the bottom link which can turn the double pendulum into a single pendulum by fixing the upper and lower links together.

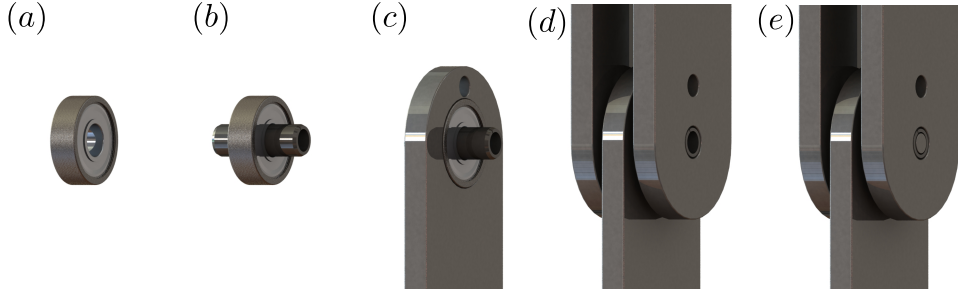


Figure 3: Assembly process for lower joint. (a) the lower bearing, (b) the hollow dowel pin pressure fit into lower bearing, (c) the lower link pressure fit into lower bearing, (d) the upper links pressure fit into hollow dowel pin, and (e) a secondary dowel pin pressed into hollow dowel pin to prevent slipping.

3.2 Marker Design and Assembly

The markers were designed to provide point reflections for tracking. The trackers were 3D printed from PLA at 20 percent infill to minimize their weight. A simple epoxy glue was used to adhere the trackers to the desired locations (see Fig. 4(a)). A highly reflective tape was used to cover the camera facing side of the tracker to allow for a high contrast between the other pendulum surfaces and the markers. To further improve the reflective contrast of the markers, all reflective surfaces were covered in either a blue or black non-reflective tape (see Fig. 4(b)). This provides a clear contrast between other surfaces and the markers as shown in Fig. 4(c).

The location of the markers is shown in Fig. 5(a). These locations were chosen to allow for the majority of the markers to be visible at all times. This includes when the lower link is occluded by the upper link. These locations were also chosen to allow for a large variety of position vectors between markers for each link. Specifically, a sort of “web” of relative position vectors can be formed (see Fig. 5(b)). This web of relative position vectors will be used in Section 5.2.2 to calculate ϕ_1 and ϕ_2 which is the respective angle of the top link and bottom link with respect to the vertical axis.

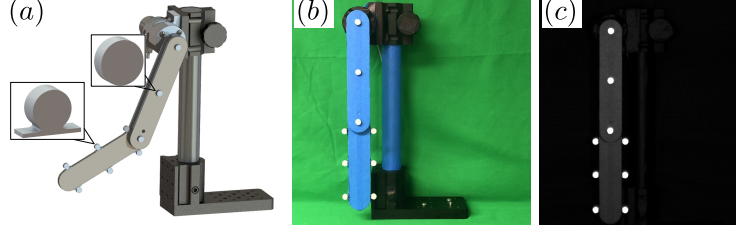


Figure 4: Marker design and assembly process. (a) Markers attached to double pendulum (see Section A.6 for mechanical drawings), (b) physical setup with tape applied to reflective surfaces of double pendulum, and (c) initial frame of video data showing high contrast between markers and the pendulum.

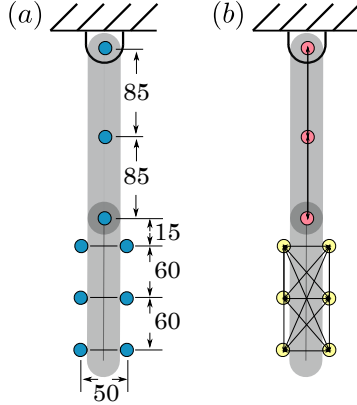


Figure 5: Marker locations. (a) Relative distances between markers and (b) web of relative position vectors for each rigid link.

4 Equations of Motion

The derivation of the detailed equations of motion (EOMs) are formulated using the Euler-Lagrange equation. To do this, the kinetic and potential energies of each moving component must be defined. The following components are considered: the encoder, upper bearing, flexible coupling, upper shaft, upper bearing, upper links, upper trackers, lower bearing, hollow dowel pin, lower bearing, lower shaft, lower link, and lower trackers. Fig. 6 shows the location of each of these components on a CAD model of the experimental double pendulum.

4.1 Component Energy Equations

Here we provide the potential (\mathcal{V}) and kinetic (\mathcal{T}) energy expressions on a component-by-component basis. In this derivation, a term \bar{I}_{\square} denotes a component's mass moment of inertia about its center of mass while I_{\square} denotes mass moment of inertia about its axis of rotation. The terms d_I and d_B denote the inner diameter of the bearing and the diameter of the bearing balls, respectively. The derivation of the energy expressions for the bearing balls is given subsequently in section A.1.

- Encoder ($\times 1$): Mass: m_1 , Inertia: $I_1 = \bar{I}_1$, Center of Mass: $X_1 = 0, Y_1 = 0$

$$\mathcal{T}_1 = \frac{1}{2} I_1 \dot{\phi}_1^2$$

$$\mathcal{V}_1 = 0$$
- Flexible Coupling ($\times 1$): Mass: m_2 , Inertia: $I_1 = \bar{I}_1$, Center of Mass: $X_2 = 0, Y_2 = 0$

$$\mathcal{T}_2 = \frac{1}{2} I_2 \dot{\phi}_1^2$$

$$\mathcal{V}_2 = 0$$
- Upper Bearing ($\times 1$):
(a) Inner Race ($\times 1$): Mass: $m_{3,1}$, Inertia: $I_{3,1} = \bar{I}_{3,1}$, Center of Mass: $X_{3,1} = 0, Y_{3,1} = 0$

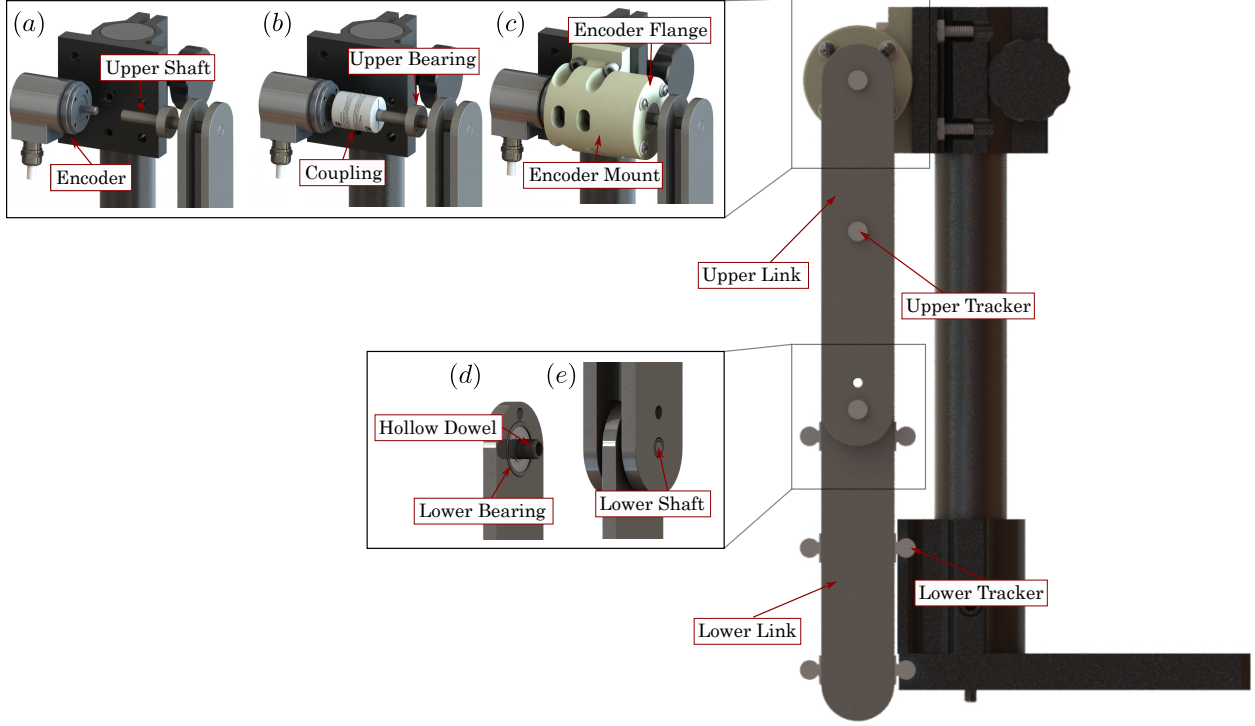


Figure 6: Dynamic components of experimental double pendulum.

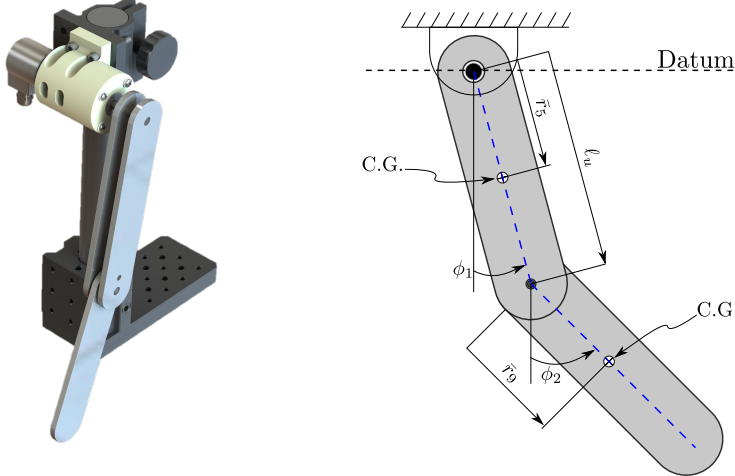


Figure 7: Configuration CAD models (left) and labels for equation derivation (right).

$$\mathcal{T}_{3,1} = \frac{1}{2} I_{3,1} \dot{\phi}_1^2$$

$$\mathcal{V}_{3,1} = 0$$

(b) Ball Spacer ($\times 1$): Mass: $m_{3,2}$, Inertia: $I_{3,2} = \bar{I}_{3,2}$, Center of Mass: $X_{3,2} = 0$, $Y_{3,2} = 0$

$$\mathcal{T}_{3,2} = \frac{1}{2} I_{3,2} \left(\frac{d_I}{2(d_I + d_B)} \dot{\phi}_1 \right)^2$$

$$\mathcal{V}_{3,2} = 0$$

(c) Bearing Ball ($\times 7$): Mass: $m_{3,3}$, Inertia: $I_{3,3} = \bar{I}_{3,3}$, Center of Mass: $X_{3,3} = 0$, $Y_{3,3} = 0$

$$\mathcal{T}_{3,3} = \frac{1}{2}m_{3,3} \left(\frac{d_I}{4}\dot{\phi}_1 \right)^2 + \frac{1}{2}I_{3,3} \left(\frac{d_I}{2d_B}\dot{\phi}_1 \right)^2$$

Potential Energy (Center of Ball Set Equals Zero): $\mathcal{V}_{3,3} = 0$

4. Upper Shaft ($\times 1$): Mass: m_4 , Inertia: $I_4 = \bar{I}_4$.

$$\mathcal{T}_4 = \frac{1}{2}I_4\dot{\phi}_1^2$$

$$\mathcal{V}_4 = m_4g\bar{r}_4(1 - \cos \phi_1)$$

5. Upper Arm ($\times 2$): Mass: m_5 , Inertia: $I_5 = \bar{I}_5 + m_5\bar{r}_5^2$, Center of Mass: $X_5 = \bar{r}_5 \sin \phi_1$, $Y_5 = -\bar{r}_5 \cos \phi_1$

$$\mathcal{T}_5 = \frac{1}{2}I_5\dot{\phi}_1^2$$

$$\mathcal{V}_5 = m_5g\bar{r}_5(1 - \cos \phi_1)$$

6. Lower Shaft ($\times 1$): Mass: m_6 , Inertia: $I_6 = \bar{I}_6 + m_6\ell_u^2$, Center of Mass: $X_6 = \ell_u \sin \phi_1$, $Y_6 = -\ell_u \cos \phi_1$

$$\mathcal{T}_6 = \frac{1}{2}I_6\dot{\phi}_1^2$$

$$\mathcal{V}_6 = m_6g\ell_u(1 - \cos \phi_1)$$

7. Dowel Pin ($\times 1$): Mass: m_7 , Inertia: $I_7 = \bar{I}_7 + m_7\ell_u^2$, Center of Mass: $X_7 = \ell_u \sin \phi_1$, $Y_7 = -\ell_u \cos \phi_1$

$$\mathcal{T}_7 = \frac{1}{2}I_7\dot{\phi}_1^2$$

$$\mathcal{V}_7 = m_7g\ell_u(1 - \cos \phi_1)$$

8. Lower Bearing ($\times 1$):

- (a) Inner Race ($\times 1$): Mass: $m_{8,1}$, Inertia: $I_{8,1} = \bar{I}_{8,1} + m_{8,1}\ell_u^2$, Center of Mass: $X_{8,1} = \ell_u \sin \phi_1$, $Y_{8,1} = -\ell_u \cos \phi_1$

$$\mathcal{T}_{8,1} = \frac{1}{2}I_{8,1}\dot{\phi}_1^2$$

$$\mathcal{V}_{8,1} = m_{8,1}g\ell_u(1 - \cos \phi_1)$$

- (b) Ball Spacer ($\times 1$): Mass: $m_{8,2}$, Inertia: $I_{8,2} = \bar{I}_{8,2} + m_{8,2}\ell_u^2$, Center of Mass: $X_{8,2} = \ell_u \sin \phi_1$, $Y_{8,2} = -\ell_u \cos \phi_1$

$$\mathcal{T}_{8,2} = \frac{1}{2}m_{8,2}(\ell_u\dot{\phi}_1)^2 + \frac{1}{2}\bar{I}_{8,2} \left(\frac{d_I}{2(d_I+d_B)}\dot{\phi}_1 + \frac{d_I+2d_B}{2(d_I+d_B)}\dot{\phi}_2 \right)^2$$

$$\mathcal{V}_{8,2} = m_{8,2}g\ell_u(1 - \cos \phi_1)$$

- (c) Bearing Balls ($\times 7$): Mass: $m_{8,3}$, Inertia: $I_{8,3} = \bar{I}_{8,3} + m_{8,3}\ell_u^2$, Center of Mass: $X_{8,3} = \ell_u \sin \phi_1$, $Y_{8,3} = -\ell_u \cos \phi_1$. Note: This expression accounts for all 7 bearing balls.

$$\begin{aligned} \mathcal{T}_{8,3} &= \frac{7}{2}m_{8,3} \left[(\ell_u\dot{\phi}_1)^2 + \left(\frac{d_I}{4}\dot{\phi}_1 + \frac{d_I+2d_B}{4}\dot{\phi}_2 \right)^2 \right. \\ &\quad \left. (\ell_u\dot{\phi}_1) \left(\frac{d_I}{2(d_I+d_B)}\dot{\phi}_1 + \frac{d_I+2d_B}{2(d_I+d_B)}\dot{\phi}_2 \right) (d_I + d_B) \sum_{i=1}^7 \cos \left(\frac{2\pi(i-1)}{7} + (\theta_i - \phi_1) \right) \right] \\ &\quad + \frac{7}{2}I_{8,3} \left(\frac{d_I}{2d_B}\dot{\phi}_1 - \frac{(d_I+2d_B)}{2d_B}\dot{\phi}_2 \right)^2 \\ \mathcal{V}_{8,3} &= 7m_{8,3}g\ell_u(1 - \cos \phi_1) \end{aligned}$$

- (d) Outer Race ($\times 1$): Mass: $m_{8,4}$, Inertia: $I_{8,4} = \bar{I}_{8,4} + m_{8,4}\ell_u^2$, Center of Mass: $X_{8,4} = \ell_u \sin \phi_1$, $Y_{8,4} = -\ell_u \cos \phi_1$

$$\mathcal{T}_{8,4} = \frac{1}{2}m_{8,4}(\ell_u\dot{\phi}_1)^2 + \frac{1}{2}\bar{I}_{8,4}\dot{\phi}_2^2$$

$$\mathcal{V}_{8,4} = m_{8,4}g\ell_u(1 - \cos \phi_1)$$

9. Lower Arm ($\times 1$): Mass: m_9 , Inertia: $I_9 = \bar{I}_9 + m_9 [(\ell_u \cos \phi_1 + \bar{r}_9 \cos \phi_2)^2 + (\ell_u \sin \phi_1 + \bar{r}_9 \sin \phi_2)^2]$, Center of Mass: $X_9 = \ell_u \sin \phi_1 + \bar{r}_9 \sin \phi_2$, $Y_9 = -\ell_u \cos \phi_1 - \bar{r}_9 \cos \phi_2$

$$\mathcal{T}_9 = \frac{1}{2}m_9\ell_u^2\dot{\phi}_1^2 + m_9\ell_u\bar{r}_9\dot{\phi}_1\dot{\phi}_2 \cos(\phi_2 - \phi_1) + \frac{1}{2}m_9\bar{r}_9^2\dot{\phi}_2^2 + \frac{1}{2}\bar{I}_9\dot{\phi}_2^2$$

$$\mathcal{V}_9 = m_9g[\ell_u(1 - \cos \phi_1) + \bar{r}_9(1 - \cos \phi_2)]$$

10. Upper Trackers ($\times 3$): Mass: m_{10} , Inertia: $I_{10} = \bar{I}_{10} + m_{10}\bar{r}_{10,i}^2$, Center of Mass: $[X_{10,i}, Y_{10,i}]$ is dependent on marker location relative to link.

$$\mathcal{T}_{10} = \frac{1}{2}I_{10}\dot{\phi}_1^2$$

$$\mathcal{V}_{10} = m_{10}g\bar{r}_{10}(1 - \cos \phi_1)$$

11. Lower Trackers ($\times 6$): Mass: m_{11} , Center of Mass: $[X_{10,i}, Y_{10,i}]$ is dependent on marker location relative to link, Inertia: $I_{11} = \bar{I}_{11} + m_{11} [(\ell_u \cos \phi_1 + \bar{r}_{11} \cos \phi_2)^2 + (\ell_u \sin \phi_1 + \bar{r}_{11} \sin \phi_2)^2]$.

$$\begin{aligned}\mathcal{T}_{11} &= \frac{1}{2}m_{11}\ell_u^2\dot{\phi}_1^2 + m_{11}\ell_u\bar{r}_{11}\dot{\phi}_1\dot{\phi}_2 \cos(\phi_2 - \phi_1) + \frac{1}{2}m_{11}\bar{r}_{11}^2\dot{\phi}_2^2 + \frac{1}{2}\bar{I}_{11}\dot{\phi}_2^2 \\ \mathcal{V}_{11} &= m_{11}g[\ell_u(1 - \cos \phi_1) + \bar{r}_{11}(1 - \cos \phi_2)]\end{aligned}$$

12. Upper Arm Tape ($\times 1$): Mass: m_{12} , Inertia: $I_{12} = \bar{I}_{12} + m_{12}\bar{r}_{12}^2$, Center of Mass: $X_{12} = \bar{r}_{12} \sin \phi_1$, $Y_{12} = -\bar{r}_{12} \cos \phi_1$

$$\begin{aligned}\mathcal{T}_{12} &= \frac{1}{2}I_{12}\dot{\phi}_1^2 \\ \mathcal{V}_{12} &= m_{12}g\bar{r}_{12}(1 - \cos \phi_1)\end{aligned}$$

13. Lower Arm Tape ($\times 1$): Mass: m_{13} , Center of Mass: $X_{13} = \ell_u \sin \phi_1 + \bar{r}_{13} \sin \phi_2$, $Y_{13} = -\ell_u \cos \phi_1 - \bar{r}_{13} \cos \phi_2$, Inertia: $I_{13} = \bar{I}_{13} + m_{13} [(\ell_u \cos \phi_1 + \bar{r}_{13} \cos \phi_2)^2 + (\ell_u \sin \phi_1 + \bar{r}_{13} \sin \phi_2)^2]$.

$$\begin{aligned}\mathcal{T}_{13} &= \frac{1}{2}m_{13}\ell_u^2\dot{\phi}_1^2 + m_{13}\ell_u\bar{r}_{13}\dot{\phi}_1\dot{\phi}_2 \cos(\phi_2 - \phi_1) + \frac{1}{2}m_{13}\bar{r}_{13}^2\dot{\phi}_2^2 + \frac{1}{2}\bar{I}_{13}\dot{\phi}_2^2 \\ \mathcal{V}_{13} &= m_{13}g[\ell_u(1 - \cos \phi_1) + \bar{r}_{13}(1 - \cos \phi_2)]\end{aligned}$$

With these expressions, we can now account for the energy of any moving component. It may be of interest to some how the equations for the potential and kinetic energy of the bearing balls were contrived, specifically $\mathcal{T}_{8,3}$. Before moving into the governing EOM for the entire system, we provide this derivation in the appendix of this document.

4.2 Equations of motion

The total kinetic energy of this system is now given with

$$\begin{aligned}\mathcal{T} &= \mathcal{T}_1 + \mathcal{T}_2 + 2(\mathcal{T}_{3,1} + \mathcal{T}_{3,2} + \mathcal{T}_{3,3}) + \mathcal{T}_4 + 2\mathcal{T}_5 + \mathcal{T}_6 + \mathcal{T}_7 + (\mathcal{T}_{8,1} + \mathcal{T}_{8,2} + \mathcal{T}_{8,3} + \mathcal{T}_{8,4}) + \mathcal{T}_9 \\ &\quad + \sum \mathcal{T}_{10,i} + \sum \mathcal{T}_{11,i} + \mathcal{T}_{12} + \mathcal{T}_{13},\end{aligned}\quad (1)$$

and the total potential energy is given with

$$\begin{aligned}\mathcal{V} &= \mathcal{V}_1 + \mathcal{V}_2 + 2(\mathcal{V}_{3,1} + \mathcal{V}_{3,2} + \mathcal{V}_{3,3}) + \mathcal{V}_4 + 2\mathcal{V}_5 + \mathcal{V}_6 + \mathcal{V}_7 + (\mathcal{V}_{8,1} + \mathcal{V}_{8,2} + \mathcal{V}_{8,3} + \mathcal{V}_{8,4}) + \mathcal{V}_9 \\ &\quad + \sum \mathcal{V}_{10,i} + \sum \mathcal{V}_{11,i} + \mathcal{V}_{12} + \mathcal{V}_{13}.\end{aligned}\quad (2)$$

By combining the potential and kinetic energies, the total energy as a function of ϕ_1 , ϕ_2 , $\dot{\phi}_1$, and $\dot{\phi}_2$ is

$$E = \mathcal{T} = \mathcal{V} \quad (3)$$

However, to determine the EOM, Lagrange's equation will be implemented, which requires the Lagrangian. The Lagrangian of the system is defined as

$$\mathcal{L} = \mathcal{T} - \mathcal{V} \quad (4)$$

Lagrange's equations is then applied to the system to for the equation of motion for the upper and lower link as

$$\begin{aligned}\frac{d}{dt} \left(\frac{\partial \mathcal{L}}{\partial \dot{\phi}_1} \right) - \frac{\partial \mathcal{L}}{\partial \phi_1} + M_v^{(i)} + M_q^{(i)} + M_c^{(i)} &= 0, \\ \frac{d}{dt} \left(\frac{\partial \mathcal{L}}{\partial \dot{\phi}_2} \right) - \frac{\partial \mathcal{L}}{\partial \phi_2} + M_v^{(i)} + M_q^{(i)} + M_c^{(i)} &= 0,\end{aligned}\quad (5)$$

where M_v , M_q , and M_c are the damping moments from viscous, quadratic, and Coulomb damping. The expanded and exact expressions for these damping moments are developed in Section 6.1.

For the bearing balls, it is neater to write the kinetic energy term with respect to the variable Λ . We define Λ as $\sum_{i=1}^9 \cos \left(\frac{2\pi(i-1)}{9} + (\theta_1 - \phi_1) \right)$. Note that even with the introduction of Λ , the potential energy \mathcal{T}_{73} holds its original definition. Substituting this new term into the equation for the kinetic energy in the bearing balls of the lower bearings, the energy expressions for these components become:

$$\begin{aligned} \mathcal{T}_{8,3} = & \frac{7}{2} \bar{I}_{8,3} \left(\frac{\dot{\phi}_2 (2d_B + d_I)}{2d_B} - \frac{d_I \dot{\phi}_1}{2d_B} \right)^2 + \frac{7}{2} m_{8,3} \left[\left(\frac{d_I \dot{\phi}_1}{4} + \dot{\phi}_1 \left(\frac{d_B}{2} + \frac{d_I}{4} \right) \right)^2 + \right. \\ & \left. \dot{\phi}_1^2 \ell_u^2 + \dot{\phi}_2 \ell_u (d_B + d_I) \left(\frac{d_I \dot{\phi}_1}{2} + \dot{\phi}_2 \left(d_B + \frac{d_I}{2} \right) \right) \Lambda \right] \quad (6) \end{aligned}$$

Where $\Lambda = \Lambda(\phi_1, \Delta\phi_1, \Delta\phi_2)$ and both $\Delta\phi_1$ and $\Delta\phi_2$ are functions of time

The equations of motion may be written in terms of fewer variables by grouping together variables which are invariant of time, arm position, and arm velocities, there is a great reduction in the number of variables required to express the same equations of motion. Furthermore, if we ignore the variable Λ , the equations are reduced even more. Ignoring Λ the energy equations may be written as:

$$T = \psi \dot{\phi}_1^2 + \lambda \dot{\phi}_2^2 + (\zeta + A_3, \cos(\phi_2 - \phi_1)) \dot{\phi}_1 \dot{\phi}_2 \quad (7)$$

$$V = \sigma (1 - \cos \phi_1) + \kappa (1 - \cos \phi_2) \quad (8)$$

Then, by applying Eq. (5) to the reduced energy expressions, the equations of motion without damping become

$$0 = 2\psi \ddot{\phi}_1 + \zeta \ddot{\phi}_2 + \sigma \sin(\phi_1) + A_3, \sin(\phi_1 - \phi_2) \dot{\phi}_2^2 + A_3, \cos(\phi_1 - \phi_2) \ddot{\phi}_2 + M_v^{(i)} + M_q^{(i)} + M_c^{(i)} \quad (9)$$

$$0 = 2\lambda \ddot{\phi}_2 + \zeta \ddot{\phi}_1 + \kappa \sin(\phi_2) - A_3, \sin(\phi_1 - \phi_2) \dot{\phi}_1^2 + A_3, \cos(\phi_1 - \phi_2) \ddot{\phi}_1 + M_v^{(i)} + M_q^{(i)} + M_c^{(i)} \quad (10)$$

Note that the definitions of $\psi, \kappa, \sigma, \zeta$ and A_1, A_2, A_3 are given in Tab. 9. The uncertainties of these terms are given as well. We now have a easily workable equation of motion to describe the dynamics of each moving component within the assembly. Thus, Eqs. (9) and (10) are used for simulations of the system.

5 Data Collection and Analysis

In this study, two methods are used to cross validate the experimental data. First, encoder data is recorded from angle of the top link ϕ_1 as a raw voltage output from 0 – 10 V. The calibration and verification of the encoder data is discussed in Section 5.1. For the second method, video data is recorded a processed using the method and algorithm discussed in Section 5.2.

5.1 Encoder Data Collection and Calibration

To begin the data collection process, the output from the encoder was connect to an analog input pin from on the DAQ and the encoder was power with 24 V with the power supply. The output from the encoder ranges from 0-10 V with approximately 0.65 V per full revolution. This encoder allows for the pendulum to rotate multiple times without exceeding the rotational bounds. The recording rate was set to 500 Hz to sufficiently capture the dynamics of the double pendulum.

The only step needed to analyze the raw voltage data is to calibrate the encoder between angle and voltage. To do this, seven data points were taken at intervals of full rotations from an original downward configuration considered zero position at approximately the 5 V location. At each downward configuration, it is assumed that the angle has no error and thus include the angles $\phi = [-1080^\circ, -720^\circ, -360^\circ, 0^\circ, 360^\circ, 720^\circ, 1080^\circ]$. The corresponding voltage at each downward configuration was then recorded for 3 seconds at a rate of 500 Hz to allow for the calculation of the mean and standard deviation at each. The resulting calibration points are shown in Fig. 8, which shows a highly linear relationship between voltage and angle. Additionally, a zoomed in point at the positive 360° location shows that the standard deviation of the voltage falls within the 2.5 mV specified uncertainty of the encoder.

5.2 Video Data Collection and Calibration

To analyze the double pendulum using video data, multiple point markers were used to track the angular position of each link. The marker design is discussed in Section 3.2. The design causes for high reflectivity at

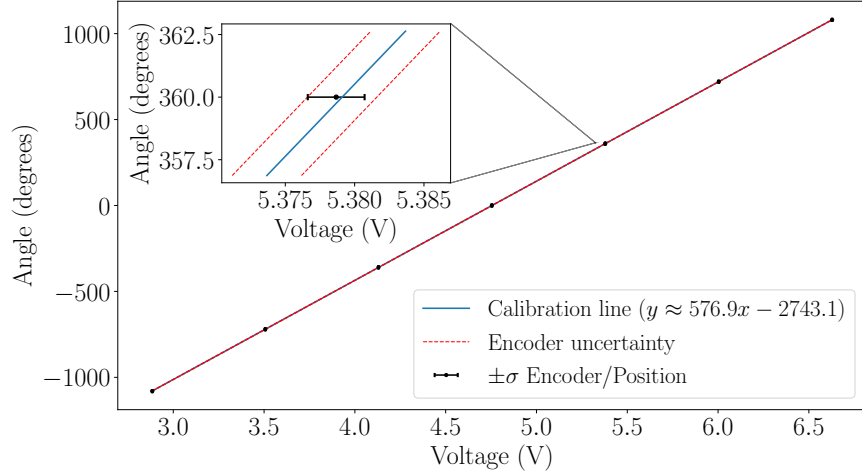


Figure 8: Calibration line for the encoder used to measure the angle of the top link of the double pendulum.

the markers or points of interest. These markers are also referred to as nodes in the following sections. The reflective nature in comparison to the surroundings (see Fig. 9 a) allows for the use of the *moments* function openCV, which provides the approximate center of each marker. Figure 9 b shows the output location of each node marked with its respective letter (A, B, C,...). Unfortunately, keeping track of the markers through

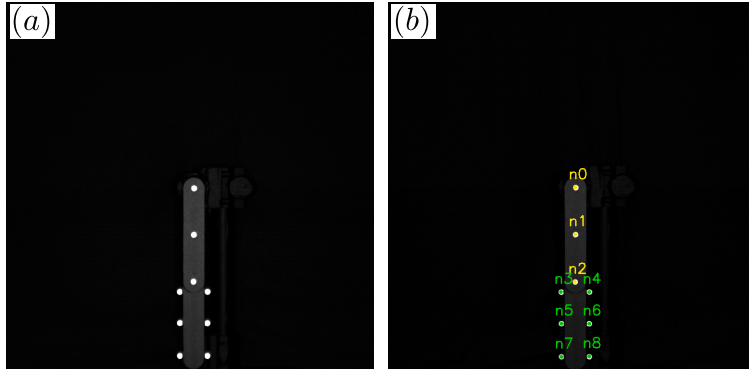


Figure 9: Double pendulum marker function and node locating. (a) shows the high contrast locations at the markers and (b) shows the location output from using the center of the moment contours from openCV.

consecutive frames is a challenging task. It is made even more so by the common occurrence of occlusions with the lower link swinging behind the upper link. To account for this, Section A.4 discusses a tracking algorithm for rigid bodies we developed, which, in brief, uses the nearest neighbors of each node that is part of its respective rigid body to reassign the node through occlusions. In Section 5.2.1 we will propose a method for calculating ϕ for a simple pendulum based on minimizing the error in the calculation. Following, in Section 5.2.2, the method will be applied to calculate both ϕ_1 and ϕ_2 .

5.2.1 Pendulum Error Analysis for Video Data

For simplicity, we will only show the error analysis for the single pendulum as the general rule will apply to both single and double pendulums. For our analysis, we will compare two ways of determining ϕ . The first (see left of Fig. 10) directly measures ϕ from a reference vector v_{ref} , and the second (see right of Fig. 10) uses the change in angle between concurrent frames $\Delta\phi$ with ϕ being calculated using the summation of all previous $\Delta\phi$ over a total of T frames as $\phi = \sum_i^T \Delta\phi_i$. While both methods will work for determining ϕ if there is no noise in the system, it was found that the first method (left side of Fig. 10) avoids a compounding error, which is prevalent even with small amounts of noise. A full discussion of the error analysis is provided in Section A.4.1

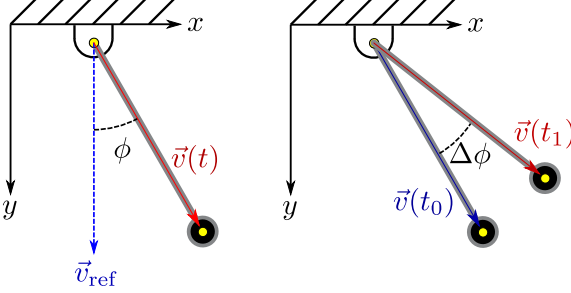


Figure 10: Visual representation of two methods for calculating ϕ using video data described in Section A.4.1.

5.2.2 Pendulum Measurements Using Video Data

This section describes the reasoning for the method used for calculating the upper link's angle to vertical ϕ_1 and the lower links angle to vertical ϕ_2 of a double pendulum as shown on the right side of Fig. 11. To begin, a node assignment is placed on each marker on the pendulum for reference to which rigid body the node belongs to (see left side of Fig. 11) with the upper link having $[n_0, n_1, n_2] \in \mathbf{L}_1$ and the lower link having $[n_3, n_4, n_5, n_6, n_7, n_8] \in \mathbf{L}_2$. Using the rigid body node assignment, position vectors between nodes for the

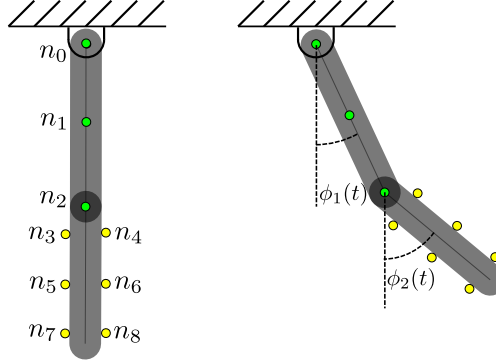


Figure 11: Double pendulum diagram showing node assignment on the left and ϕ_1 and ϕ_2 reference on the right.

upper and lower links are calculated as

$$\begin{aligned} \vec{p}_{j/i}(t) &= [x_j(t) - x_i(t), y_j(t) - y_i(t)] \\ &= [x_{j/i}(t), y_{j/i}(t)] \end{aligned} \quad (11)$$

where only the direction is considered if the source node n_i and sink node n_j are such that $j > i$ and nodes n_i and n_j are part of the same link. This is done to avoid repeated vectors that are opposite in direction. Using all the possible vector combinations in each link, the angle between the original position vector $\vec{p}_{j/i}(0)$ and the configuration at a later time $\vec{p}_{j/i}(t)$ is used to calculate the angle between the two as

$$\phi_L^{(i,j)}(t) = \tan^{-1} \left(\frac{y_{j/i}(t)}{x_{j/i}(t)} \right) - \tan^{-1} \left(\frac{y_{j/i}(0)}{x_{j/i}(0)} \right), \quad (12)$$

where \tan is $\arctan 2$ to allow for the correct angle sign for all quadrants. A toy example of this process is shown in Fig. 12 with the vector from node n_3 to node n_4 at time t and $t = 0$ with a down configuration.

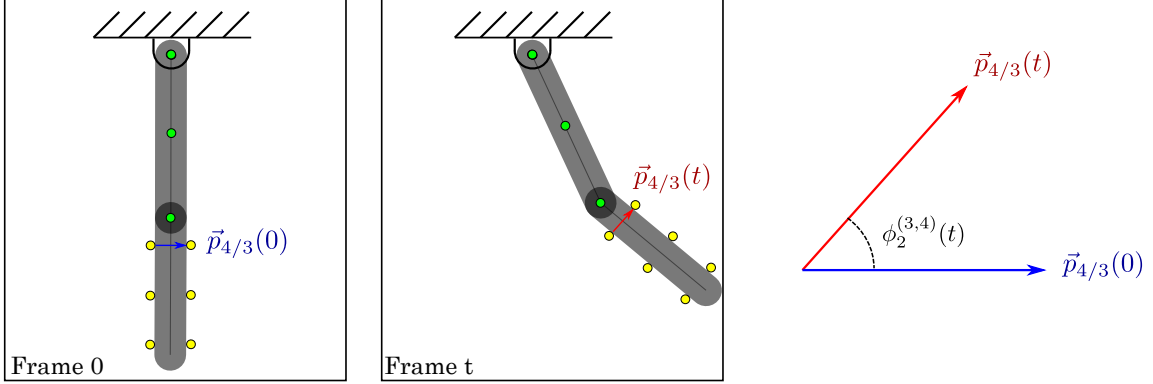


Figure 12: Example showing how $\phi_2(t)$ is found using the original down configuration and a later configuration at time t for the vector between nodes n_3 and n_4 .

This process is applied for all configuration and the mean angle $\mu_\phi(t)$ and standard deviation $\sigma_\phi(t)$ are calculated as

$$\begin{aligned} \mu_\phi(t) &= \frac{1}{N} \sum_{(i,j)} \phi_L^{(i,j)}(t), \\ \sigma_\phi(t) &= \sqrt{\frac{1}{N} \sum_{(i,j)} [\mu_\phi(t) - \phi_L^{(i,j)}(t)]^2}. \end{aligned} \quad (13)$$

6 Data Validation

To validate the video data, a cross reference to the encoder data was done. The cross reference was in regards to the calibrated encoder data as the encoder will serve as a ground truth for the calibrated video data comparison. The data was collected from a simple free drop from approximate initial conditions of $[\theta_1, \dot{\theta}_2, \theta_2, \dot{\theta}_2] = [180^\circ, 0, 180^\circ, 0]$. However, before the comparison could be made, the video and encoder data needed to be synchronized. To do this, we implemented the synchronization software provided by Photron implemented in *Potron FASTCAM Viewer 4* or PFV4. Specifically, the add-on *DAQ control* was used to synchronize the video data to the input channels, including the encoder, on the DAQ. This add-on allowed for each frame to be associated with each recording from the DAQ, which insured a direct comparison between the calibrated encoder and analyzed video data could be made. For the sake of simplicity, only a subjective, visual confirmation will be used to validate the video data. To do this, a zoomed-in section of the encoder data overlaid with the video data were analyzed as shown in Fig. 13. As shown in the left-hand-side of Fig. 13, the time series from both encoder and video show, in general, similar amplitude and synchronization. To better examine the differences between the time series, the top and bottom figures on the right side of Fig. 13 further show that the amplitude and synchronization agree very well between the two data source. Additionally, the bottom right figure shows that the video data has greater precision than the calibrated encoder data for θ_1 . This demonstrates that the video data is an accurate method for capturing both θ_1 and θ_2 for the double pendulum. To further demonstrate the improved precision of the video data in comparison to high-quality encoder data, Fig. 14 shows both the mean values of θ_1 and θ_2 as well as their uncertainties, $\sigma\theta_1$ and $\sigma\theta_2$.

6.1 Damping Parameter Estimation

To estimate the optimum damping parameters for the double pendulum simulation, three models were investigated. These models are viscous damping in the bearings, quadratic damping from fluid dynamics, and Coulomb damping in the bearings. These damping models are summarized in Table 4 as moments impeding motion on the upper and lower links respectively.

While the viscous and quadratic energy losses can be calculated using the collected data for ϕ_1 and ϕ_2 , the Coulomb damping expression requires the normal force associated with each joint in the double pendulum. To do this, it is assumed that the double pendulum can be effectively reduced to the simple two link double

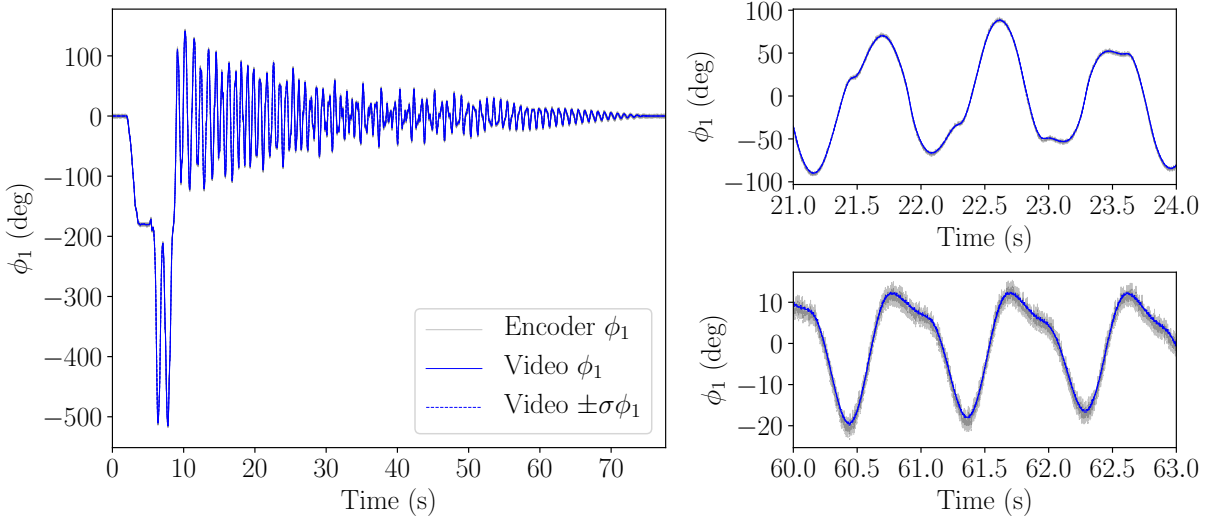


Figure 13: Comparison between synchronized encoder and video data of θ_1 for validation of video data. (left) entire time series of recorded data from both encoder and video data, (top right) zoomed-in section of time series at $t \in [21, 24]$, and (bottom right) zoomed-in section of time series at $t \in [60, 63]$. $\pm\sigma\theta_1$ representations a one standard in the calculation for θ_1 using the video data.

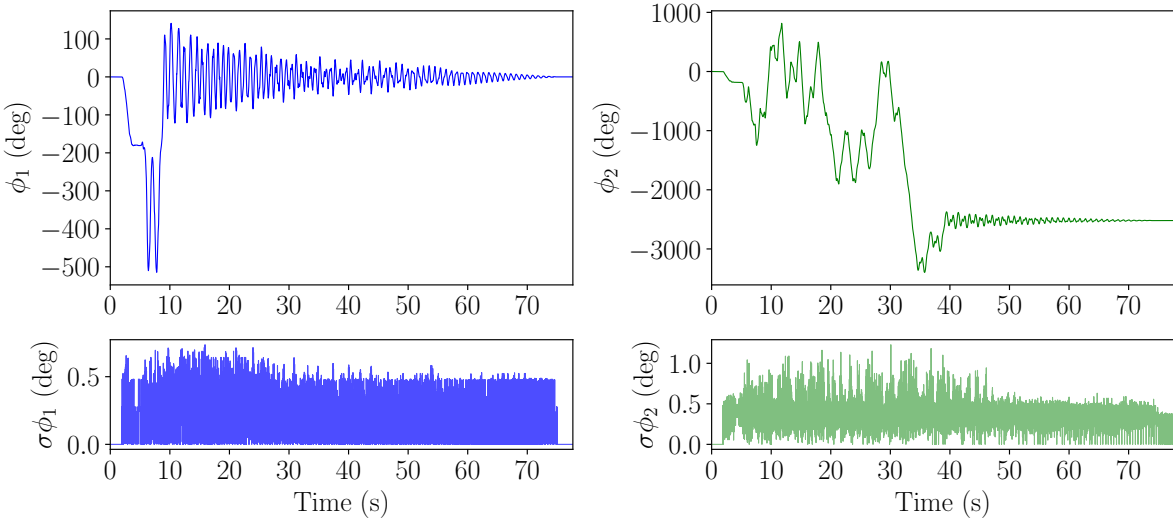


Figure 14: Analyzed video data for θ_1 and θ_2 of a free drop double pendulum with associated standard deviation of calculation for θ_1 and θ_2 underneath.

pendulum shown in Fig. 15. This assumption should hold true as all of the components of the experimental double pendulum are symmetric about the link and are rigidly attached to each link separately. The only exception to this are the balls in the lower bearing, which move with respect to both the upper and link rotation, separately. Due to the minimal influence from a relatively small mass of the bearing balls, they will be ignored in the derivation of the normal forces. The joint normal force derivation will begin by applying Newton's law of motion on the upper and lower links separately in the x and y directions with the Free Body Diagrams (FBD) shown in Fig. 16. The acceleration of the Center of Gravity (CG) of each link is calculated by taking the second time derivative of their positions given by $p_1 = [d_1 \sin(\phi_1), -d_1 \cos(\phi_1)]$ and $p_2 = [\ell_1 \sin(\phi_1) + d_2 \sin(\phi_2), -\ell_1 \cos(\phi_1) - d_2 \cos(\phi_2)]$ for the upper and lower links, respectively. Next, by applying Newton's law of motion in the x and y directions for both the upper and lower links, the tension

Table 4: Non-conservative damping models used for estimating damping in experimental double pendulum.

Damping Model	Damping Moment	Energy Loss
Viscous	$M_v = \mu_v \dot{\phi}$	$E_v = \int_0^t M_v \dot{\phi} dt$
Quadratic	$M_q = \mu_q \dot{\phi} \dot{\phi}$	$E_q = \int_0^t M_q \dot{\phi} dt$
Coulomb	$M_c = \mu_c N r \operatorname{sgn}(\dot{\phi})$	$E_c = \int_0^t M_c \dot{\phi} dt$

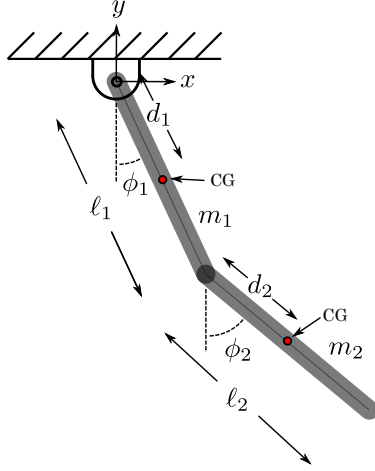


Figure 15: Reduced double pendulum model for two simple, symmetric links.

terms in the upper and lower joints ($T_{x1}, T_{y1}, T_{x2}, T_{y2}$) were solved for as

$$\begin{aligned} T_{x1} &= (d_1 + \ell_1) [-\sin(\phi_1)\dot{\phi}_1^2 + \cos(\phi_1)\ddot{\phi}_1] + d_2 [-\sin(\phi_2)\dot{\phi}_2^2 + \cos(\phi_2)\ddot{\phi}_2], \\ T_{y1} &= (m_1 + m_2)g + (d_1 + \ell_1) [\cos(\phi_1)\dot{\phi}_1^2 + \sin(\phi_1)\ddot{\phi}_1] + d_2 [\cos(\phi_2)\dot{\phi}_2^2 + \sin(\phi_2)\ddot{\phi}_2], \\ T_{x2} &= \ell_1 [-\sin(\phi_1)\dot{\phi}_1^2 + \cos(\phi_1)\ddot{\phi}_1] + d_2 [-\sin(\phi_2)\dot{\phi}_2^2 + \cos(\phi_2)\ddot{\phi}_2], \\ T_{y2} &= m_2 g + \ell_1 [\cos(\phi_1)\dot{\phi}_1^2 + \sin(\phi_1)\ddot{\phi}_1] + d_2 [\cos(\phi_2)\dot{\phi}_2^2 + \sin(\phi_2)\ddot{\phi}_2]. \end{aligned} \quad (14)$$

Using the joint tensions in Eq. (14), the magnitude of the normal force was then calculated as $N_i = \sqrt{T_x i^2 + T_y i^2}$ for both the links, resulting in the simplified normal forces

$$\begin{aligned} N_1 &= \sqrt{[a_1 f(\phi_1) + a_2 f(\phi_2)]^2 + [a_1 h(\phi_1) + a_2 h(\phi_2) + a_3]^2}, \\ N_2 &= \sqrt{[b_1 f(\phi_1) + b_2 f(\phi_2)]^2 + [b_1 h(\phi_1) + b_2 h(\phi_2) + b_3]^2}, \end{aligned} \quad (15)$$

where the constants are $a_1 = d_1 m_2 + \ell_1 m_2$, $a_2 = m_2 d_2$, $a_3 = (m_1 + m_2)g$, $b_1 = \ell_1 m_2$, $b_2 = m_2 d_2$, and $b_3 = m_2 g$ and the functions are $f(\phi) = -\sin(\phi)\dot{\phi}^2 + \cos(\phi)\ddot{\phi}$ and $h(\phi) = \cos(\phi)\dot{\phi}^2 + \sin(\phi)\ddot{\phi}$. By substituting these normal forces into the Coulomb damping expression in Table 4, the energy loss is expressed as

$$\begin{aligned} E_c^{(1)} &= \int_0^t M_c^{(1)} \dot{\phi}_1 dt, \\ E_c^{(2)} &= \int_0^t M_c^{(2)} (\dot{\phi}_2 - \dot{\phi}_1) dt, \end{aligned} \quad (16)$$

where the damping moments are

$$\begin{aligned} M_c^{(1)} &= \sqrt{\left[\mu_{c1}^{(1)} f(\phi_1) + \mu_{c2}^{(1)} f(\phi_2)\right]^2 + \left[\mu_{c1}^{(1)} h(\phi_1) + \mu_{c2}^{(1)} h(\phi_2) + \mu_{c3}^{(1)}\right]^2} \operatorname{sgn}(\dot{\phi}_1), \\ M_c^{(2)} &= \sqrt{\left[\mu_{c1}^{(2)} f(\phi_1) + \mu_{c2}^{(2)} f(\phi_2)\right]^2 + \left[\mu_{c1}^{(2)} h(\phi_1) + \mu_{c2}^{(2)} h(\phi_2) + \mu_{c3}^{(2)}\right]^2} \operatorname{sgn}(\dot{\phi}_2 - \dot{\phi}_1) \end{aligned} \quad (17)$$

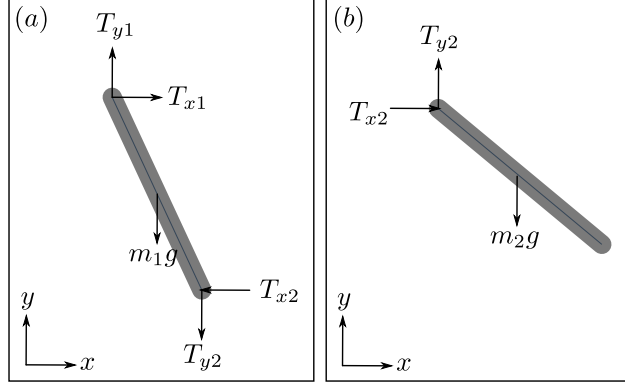


Figure 16: Free body diagrams for the (a) upper and (b) lower links.

and the constants are $\mu_{c1}^{(1)} = r\mu_c a_1$, $\mu_{c2}^{(1)} = r\mu_c a_2$, $\mu_{c3}^{(1)} = r\mu_c a_3$, $\mu_{c1}^{(2)} = r\mu_c b_1$, $\mu_{c2}^{(2)} = r\mu_c b_2$, and $\mu_{c3}^{(2)} = r\mu_c b_3$ with the superscript denoting which joint/link the constant or energy loss belongs to. The energy loss for viscous damping is calculated as

$$\begin{aligned} E_v^{(1)} &= \int_0^t \mu_v^{(1)} \dot{\phi}_1^2 dt, \\ E_v^{(2)} &= \int_0^t \mu_v^{(2)} (\dot{\phi}_2 - \dot{\phi}_1)^2 dt, \end{aligned} \quad (18)$$

where $\mu_v^{(1)}$ and $\mu_v^{(2)}$ are the viscous damping constants for the upper and lower links, respectively. Lastly, the energy loss for Quadratic damping is calculated as

$$\begin{aligned} E_q^{(1)} &= \int_0^t \mu_q^{(1)} |\dot{\phi}_1| \dot{\phi}_1^2 dt, \\ E_q^{(2)} &= \int_0^t \mu_q^{(2)} |\dot{\phi}_2| \dot{\phi}_2^2 dt, \end{aligned} \quad (19)$$

where $\mu_q^{(1)}$ and $\mu_q^{(2)}$ are the quadratic damping constants for the upper and lower links, respectively.

Using the energy loss equations (16), (18), and (19), the energy profile was optimized to fit the actual energy profile as shown in Fig. 17. Additionally, a zoomed-in section of the beginning of the energy profile in Fig. 17 shows a general matching between the simulated energy and energy from the data. A possible cause for the imperfect matching of the two energy profiles may be due to the inherent noise in the data collected, which has a more severe effect on the simulated energy profile, as it is dependent on the second time derivative of the angles. The simulated energy profile was matched by optimizing the damping constants for each damping model using the L-BFGS-R optimization method. This optimization was done for three trials. The resulting parameter values with their associated uncertainty are shown in Fig. 18.

As shown in Table 5, the magnitude of the damping coefficients is heavily weighted towards Coulomb damping. This weighting was validated by calculating the percent of the total energy dissipated by each damping method. We found that viscous, quadratic and Coulomb damping account for approximately 9%, 22%, and 69%, respectively. This concludes that the majority of the energy dissipation is from Coulomb damping in the bearings. Additionally, we calculated that approximately 81% of the energy was dissipated through the upper link and bearing, while only 19% through the lower link and bearing.

Acknowledgment

FAK acknowledges the support of the National Science Foundation under grants CMMI-1759823 and DMS-1759824.

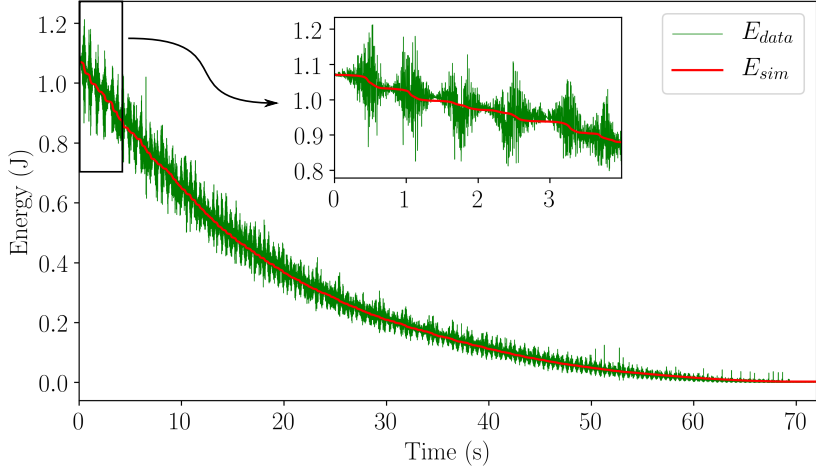


Figure 17: Zoomed-in section of the energy profile between experimental and simulated energy loss at beginning of drop.

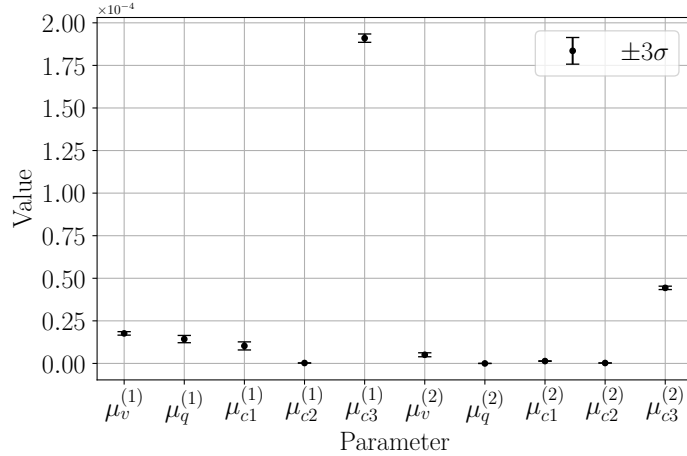


Figure 18: Damping parameter optimization results for three trials of the free-drop double pendulum.

References

- [1] A M Calvão and T J P Penna. The double pendulum: a numerical study. *European Journal of Physics*, 36(4):045018, may 2015.
- [2] Himanshu Jain, Ashish Ranjan, and Kshitij Gupta. Analysis of chaos in double pendulum. In *2013 6th International Conference on Emerging Trends in Engineering and Technology*. IEEE, dec 2013.
- [3] Jin-Wei Liang. Damping estimation via energy-dissipation method. *Journal of Sound and Vibration*, 307(1-2):349–364, oct 2007.
- [4] J. C. Sartorelli and W. Lacarbonara. Parametric resonances in a base-excited double pendulum. *Nonlinear Dynamics*, 69(4):1679–1692, mar 2012.
- [5] Troy Shinbrot, Celso Grebogi, Jack Wisdom, and James A. Yorke. Chaos in a double pendulum. *American Journal of Physics*, 60(6):491–499, jun 1992.
- [6] Tomasz Stachowiak and Toshio Okada. A numerical analysis of chaos in the double pendulum. *Chaos, Solitons & Fractals*, 29(2):417–422, jul 2006.

Table 5: Optimized damping parameters with associated uncertainty (one standard deviation) from three trials.

Parameter	Value	Uncertainty ($\pm\sigma$)
$\mu_v^{(1)}$	1.76E-05	3.42E-07
$\mu_q^{(1)}$	1.43E-05	7.24E-07
$\mu_{c1}^{(1)}$	1.03E-05	7.70E-07
$\mu_{c2}^{(1)}$	2.45E-07	5.43E-09
$\mu_{c3}^{(1)}$	1.91E-04	6.05E-07
$\mu_v^{(2)}$	5.08E-06	3.89E-07
$\mu_q^{(2)}$	0.00E+00	0.00E+00
$\mu_{c1}^{(2)}$	1.38E-06	5.37E-08
$\mu_{c2}^{(2)} = \mu_{c2}^{(1)}$	2.45E-07	5.43E-09
$\mu_{c3}^{(2)}$	4.44E-05	3.46E-07

A Additional Information

A.1 Bearing Kinematics: Velocity Analysis using Absolute velocities

In the energy expressions, the equations given for the kinetic energies of the bearing assembly components are listed. Here, we provide the development of these equations. Let d_I be the diameter of the inner race of the ball bearing, d_B the diameter of the balls, ω_D the angular velocity of axis $\hat{i}\text{-}\hat{j}$ which is attached to $\overline{OC_0}$, ω_A the angular velocity of the inner race of the bearing, and ω_c is the angular velocity of the ball bearing. Consider the velocity of point P on the inner race

$$\vec{v}_P = \vec{v}_0 + \vec{v}_{P/O} = \vec{v}_0 + \omega_A \frac{d_I}{2} \hat{i}. \quad (20)$$

If we now consider the velocity of point P' on the ball bearing which is in contact with point P at the shown instant, we obtain

$$\vec{v}_{P'} = \vec{v}_{C_0} + \vec{v}_{P'/C_0}. \quad (21)$$

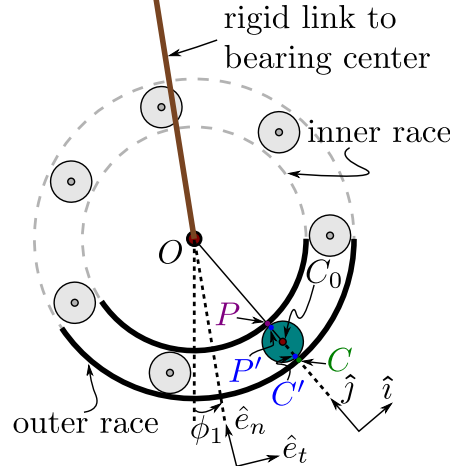


Figure 19: Schematic of the ball bearing used (the retainer ring is not shown).

But $\vec{v}_{C_0} = \vec{v}_0 + \vec{v}_{C_0/O} = \vec{v}_0 + \frac{1}{2}(d_I + d_B)\omega_D \hat{i}$, so we can write

$$\vec{v}_{P'} = \vec{v}_0 + \frac{1}{2}((d_I + d_B)\omega_D + \omega_c d_B) \hat{i}. \quad (22)$$

Using the no-slip condition implies that $\mathcal{V}_P = \mathcal{V}_{P'}$, which gives

$$\omega_A d_I = (d_I + d_B)\omega_D + d_B \omega_C. \quad (23)$$

If we now consider the velocity of point C' on the ball bearing, we can write

$$\vec{v}_{C'} = \vec{v}_{C_0} + \mathcal{V}_{C'/C_0} = \vec{v}_0 + \frac{1}{2}((d_I + d_B)\omega_D - \omega_c d_B) \hat{i}. \quad (24)$$

Point C' is in contact with point C on the outer race whose velocity is given by

$$\vec{v}_C = \vec{v}_O + \vec{v}_{C/O} = \vec{v}_0 + \frac{(d_I + 2d_B)}{2}\omega_B \hat{i} \quad (25)$$

Using the no-slip condition between points C and C' leads to $\mathcal{V}_C = \mathcal{V}_{C'}$, which gives

$$(d_I + d_B)\omega_D - d_B \omega_C = (d_I + 2d_B)\omega_B. \quad (26)$$

Adding Eqs. (23) and (26) gives

$$\omega_D = \frac{d_I}{2(d_I + d_B)}\omega_A + \frac{d_I + 2d_B}{2(d_I + d_B)}\omega_B. \quad (27)$$

Substituting the expression for ω_D from Eq. (27) into Eq. (23) gives

$$\omega_C = \frac{d_I}{2d_B}\omega_A - \frac{(d_I + 2d_B)}{2d_B}\omega_B. \quad (28)$$

The angular velocities of the inner race ω_A and the outer race ω_B depend on the double pendulum design. Figure 7 shows two alternatives a configuration for which the outer race of the bearing which couples the top and bottom links is fixed to the bottom link, while the inner race is fixed to top links. This will be dubbed configuration A. An alternative option would be to configure this linkage so that the outer race is fixed to the top link while the inner race is fixed to the bottom link. This configuration will be referred to as configuration B, and here we provide the governing equations for the bearing kinematics for both configurations.

Table 6: Angular velocity expressions for the two bearing configurations shown in Fig. 7

	configuration A	configuration B
ω_C	$\frac{d_I}{2d_B}\dot{\phi}_1 - \frac{(d_I + 2d_B)}{2d_B}\dot{\phi}_2$	$\frac{d_I}{2d_B}\dot{\phi}_2 - \frac{(d_I + 2d_B)}{2d_B}\dot{\phi}_1$
ω_D	$\frac{d_I}{2(d_I + d_B)}\dot{\phi}_1 + \frac{d_I + 2d_B}{2(d_I + d_B)}\dot{\phi}_2$	$\frac{d_I}{2(d_I + d_B)}\dot{\phi}_2 + \frac{d_I + 2d_B}{2(d_I + d_B)}\dot{\phi}_1$

A.2 Velocity Analysis using a frame attached to $\overline{OC_0}$

Denote the frame attached to the line $\overline{OC_0}$ by D . We can now write the following expressions for the angular velocities

$$\vec{\omega}_A = \omega_A \hat{k}, \quad \omega_D = \omega_D \hat{k}, \quad \omega_C = -\omega_C \hat{k}, \quad \omega_B = \omega_B \hat{k}, \quad {}^D\vec{v}_O = {}^D\vec{v}_{C_0} = \vec{0}, \quad (29)$$

where ω_B is the angular velocity of the outer race.

Using the relative angular velocity expressions $\vec{\omega}_A = \vec{\omega}_D + {}^D\vec{\omega}_A$, $\vec{\omega}_C = \vec{\omega}_D + {}^D\vec{\omega}_C$, and $\vec{\omega}_O = \vec{\omega}_D + {}^D\vec{\omega}_O$ we can get the relative angular velocities

$${}^D\vec{\omega}_A = \vec{\omega}_A - \vec{\omega}_D, \quad {}^D\vec{\omega}_C = \vec{\omega}_C - \vec{\omega}_D, \quad {}^D\vec{\omega}_O = \vec{\omega}_O - \vec{\omega}_D. \quad (30)$$

We can now write the expressions for the velocities of the points P and P' in reference D according to

$${}^D\vec{v}_P = {}^D\vec{v}_O + {}^D\vec{v}_{P/O} = {}^D\vec{\omega}_A \times \vec{r}_{P/O} = (\omega_A - \omega_D) \frac{d_I}{2} \hat{i}, \quad (31)$$

$${}^D\vec{v}_{P'} = {}^D\vec{v}_{C_0} + {}^D\vec{v}_{P'/C_0} = {}^D\vec{\omega}_C \times \vec{r}_{P'/C_0} = (\omega_C - \omega_D) \frac{d_B}{2} \hat{i}. \quad (32)$$

The no-slip boundary condition requires that ${}^D\vec{v}_P = {}^D\vec{v}_{P'}$, which gives

$$(\omega_A - \omega_D) \frac{d_I}{2} = (\omega_C - \omega_D) \frac{d_B}{2}. \quad (33)$$

Similarly, we can write the velocities of the points C and C' in frame D according to

$${}^D\vec{v}_C = {}^D\vec{v}_O + {}^D\vec{v}_{C/O} = {}^D\vec{\omega}_O \times -\vec{r}_{C/O} = (\omega_B - \omega_D) \left(\frac{d_I}{2} + d_B \right) \hat{i}, \quad (34)$$

$${}^D\vec{v}_{C'} = {}^D\vec{v}_{C_0} + {}^D\vec{v}_{C'/C_0} = {}^D\vec{\omega}_C \times \vec{r}_{C'/C_0} = -(\omega_C - \omega_D) \frac{d_B}{2} \hat{i}. \quad (35)$$

Enforcing the no-slip condition at the $C - C'$ contact implies that ${}^D\vec{v}_C = {}^D\vec{v}'_C$ which gives

$$-(\omega_C - \omega_D) \frac{d_B}{2} = (\omega_B - \omega_D) \left(\frac{d_I}{2} + d_B \right). \quad (36)$$

Solving Eqs. (33) and (36) for ω_D and ω_C gives the same expressions derived in Eqs. (27) and (28).

A.3 Uncertainty in the Bearing Ball Locations

Let us denote the reference bearing ball as the one which at the beginning of motion is located in $[0, \frac{2\pi}{N}]$, where N is the number of balls. The subsequent location of the reference ball can be tracked using the angle η which is measured relative to the fixed \hat{I} (or \hat{J}) axis, and is positive counterclockwise. Assuming rolling without slipping, the motion of the n th bearing ball can be found relative to the reference one using

$$\eta_n = \eta + n \frac{2\pi}{N}, \quad n = 1, 2, \dots, N-1. \quad (37)$$

We know that the angular velocity of the line connecting the centers of the bearing and the reference ball is $\dot{\eta} = \omega_D$, so using direct integration and Eq. (27) yields

$$\eta = \eta_0 + \frac{d_I}{2(d_I + d_B)} \Delta\phi_A + \frac{d_I + 2d_B}{2(d_I + d_B)} \Delta\phi_B, \quad (38)$$

where $\Delta\phi = \phi - \phi_0$, ϕ_A and ϕ_B are the angles of rotation of the inner and the outer races, respectively, while $\eta_0 \sim U(0, \frac{2\pi}{N})$ is a uniformly distributed random variable which represents the position of the reference ball at the start of motion. Consequently, η and η_n are also random variables whose distribution is not known a-priori.

A.4 Multiple Object Tracking with Occlusions Algorithm

The main challenge for processing the video data is Multiple Object Tracking (MOT) with occlusions.

One of the most common methods for doing multiple object tracking is through Kalman filters, but the method requires unique characteristics between each object being tracked and a physical model constraint (usually constant acceleration or velocity). Unfortunately, the double pendulum does not adhere to either of those requirements, which would make implementing one of these existing methods difficult. To circumvent this issue, we develop a new method using a nearest neighbor algorithm.

The method developed uses a Nearest Neighbor (NN) algorithm for both tracking the position of each node through consecutive frames and identifying a reappeared node through occlusions. Before describing the method, a list of assumptions, benefits, and drawbacks of the method are provided:

- Assumptions:
 1. The method needs enough nodes visible at all times to distinguish between missing nodes when a reappearance occurs. Specifically, the number of nodes needs to be great enough to have unique NN sequences for each missing node. This can be improved with a unique geometric layout of nodes.
 2. The objects being tracked must be approximately rigid bodies as to allow for the nearest neighbor matrix for each body to stay constant throughout the video.
- Benefits:

1. The method is not dependent on a model, and thus works well for nonlinear motion with inclusions.
 2. The method does not require a model or parameter tuning to function accurately.
- Drawbacks:
 1. The method requires the user to specify which nodes belong to which rigid body and an initial frame to generate the NN matrix where all nodes are visible. This initial frame will be used as the reference frame.
 2. The method will fail if the majority of nodes belonging to a rigid body disappear. Or in other words, the method will fail if so many nodes are missing that not all NN sequences for each missing node are unique.

The method functions by first forming a NN matrix when all nodes are visible (see left-most side of Fig. 20). Then, between frames, the first NN for all nodes in frame t and $t - 1$ are used to find the updated location of each node between sequential frames. Next, if a node disappears, the NN matrix is modified to replace any reference to that node as numpy's None, and the node that disappeared is appended to a list of missing nodes (see the second configuration in Fig. 20). When a node reappears, the NNs for that node are calculated and compared to the modified NN matrix to find the best matched NN array (column in NN matrix). This reappearance procedure is shown in the two left-most configurations in Fig. 20.

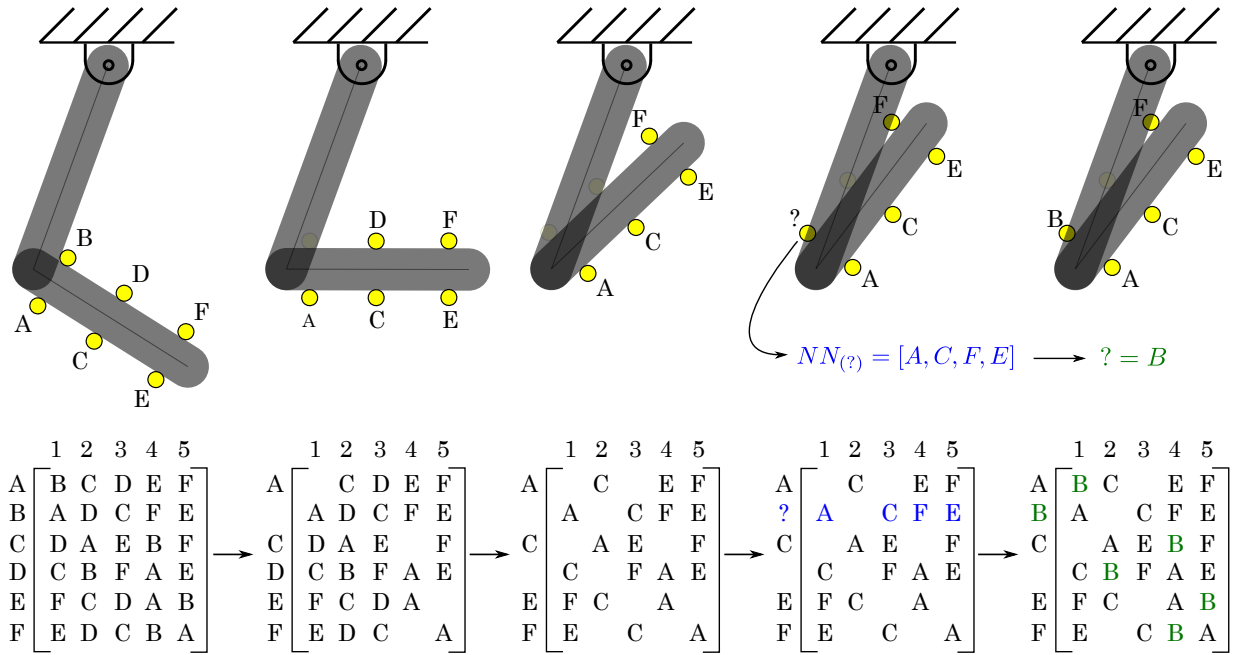


Figure 20: 2D rigidBody MOT method.

The output of this tracking method is the coordinates of each tracker relative to the frame over the entire video.

A.4.1 Pendulum Error Analysis Details

The error comparison between the two methods for calculating θ discussed in Section 5.2.1 will be provided in the subsequent paragraphs. Please reference Fig. 10 for an illustration of the two methods.

Error Analysis for Method 2 The first error analysis will be on the calculation of θ using a reference vector v_{ref} , which is calculated as

$$\theta = \tan^{-1} \left(\frac{y(t)}{x(t)} \right) - \tan^{-1} \left(\frac{y_{\text{ref}}}{x_{\text{ref}}} \right), \quad (39)$$

Next, the uncertainty is calculated as

$$\delta\theta = \sqrt{\left(\frac{\partial\theta}{\partial x_{\text{ref}}}\partial x_{\text{ref}}\right)^2 + \left(\frac{\partial\theta}{\partial y_{\text{ref}}}\partial y_{\text{ref}}\right)^2 + \left(\frac{\partial\theta}{\partial x(t)}\partial x(t)\right)^2 + \left(\frac{\partial\theta}{\partial y(t)}\partial y(t)\right)^2}. \quad (40)$$

This concludes the uncertainty analysis for method 1.

Error Analysis for Method 2 As a second method for calculating θ , we first begin by calculating the change in θ using the cross product as

$$\Delta\theta = \sin^{-1} \left(\frac{\vec{v}(t_0) \times \vec{v}(t_1)}{|\vec{v}(t_0)| |\vec{v}(t_1)|} \right), \quad (41)$$

where $\vec{v}(t_0) = [x(t_0), y(t_0)]$ and $\vec{v}(t_1) = [x(t_1), y(t_1)]$. This reduces Eq. (41) to

$$\Delta\theta = \sin^{-1} \left(\frac{x(t_0)y(t_1) - x(t_1)y(t_0)}{\sqrt{(x(t_0)^2 + y(t_0)^2)(x(t_1)^2 + y(t_1)^2)}} \right), \quad (42)$$

Additionally, there is an inherent uncertainty in both $\vec{v}(t_0)$ and $\vec{v}(t_1)$ due to the nature of video data and tracking. If this uncertainty is propagated through Eq. (42), the uncertainty can be calculated as

$$\delta\Delta\theta = \sqrt{\left(\frac{\partial\Delta\theta}{\partial x(t_0)}\partial x(t_0)\right)^2 + \left(\frac{\partial\Delta\theta}{\partial y(t_0)}\partial y(t_0)\right)^2 + \left(\frac{\partial\Delta\theta}{\partial x(t_1)}\partial x(t_1)\right)^2 + \left(\frac{\partial\Delta\theta}{\partial y(t_1)}\partial y(t_1)\right)^2}. \quad (43)$$

As shown, each $\Delta\theta$ has its own uncertainty. Now, we can use the summation of $\Delta\theta$ to find θ as

$$\theta = \sum_{i=1}^T (\Delta\theta_i + \delta\Delta\theta_i), \quad (44)$$

where T is the number of frames to go from the initial condition to the current frame. From Eq. (44), the error in θ is $\delta\theta = \sum_{i=1}^T (\delta\Delta\theta_i)$.

Error Comparison Between Methods To make a comparison between the errors introduced from each method, it is assumed that $\delta x(t_0) \approx \delta y(t_0) \approx \delta x(t_1) \approx \delta y(t_1) \approx \delta x(t) \approx \delta y(t) \approx \delta x_{\text{ref}} \approx \delta y_{\text{ref}}$. Under this assumption, $\delta\theta$ from the first method is equal to $\delta\Delta\theta$ from the second method. However, $\delta\theta$ from the second method is calculated as $\delta\theta = \sum_{i=1}^T (\delta\Delta\theta_i)$, which concludes that $\delta\theta_{\text{method 1}} = T\delta\theta_{\text{method 2}}$.

A.5 Double pendulum component measurements

Table 7: Values of overarching constants of Table 9

Constant	Calculated value	Calculated uncertainty	Unit
ψ	5470000	40000	$[g \cdot mm^2]$
λ	129000	6000	$[g \cdot mm^2]$
ζ	851	9	$[g \cdot mm^2]$
σ	681000000	5000000	$[g \cdot mm^2/s^2]$
κ	81400000	1500000	$[g \cdot mm^2/s^2]$
A_1	2000	700	$[g \cdot mm^2]$
A_2	3000	1000	$[g \cdot mm^2]$
A_3	1420000	30000	$[g \cdot mm^2]$

Table 8: Values and uncertainties of system variables

Variable	Description	Obtained with	Method	Value	Unit
m_1	Encoder mass	Not applicable	Not applicable	NA	[g]
m_2	Flex coupling	SP601 balance	Manufacturer spec.	22.3 ± 0.1	[g]
$m_{3,1}$	Bearing inner race	SP601 balance	Manufacturer spec.	2.9 ± 0.1	[g]
$m_{3,2}$	Bearing ball spacer	SP601 balance	Manufacturer spec.	0.2 ± 0.1	[g]
$m_{3,3}$	Bearing ball	SP601 balance	Manufacturer spec.	0.3 ± 0.1	[g]
m_4	Upper shaft	SP601 balance	Calculation	30 ± 0.5	[g]
m_5	Upper arm	Calculation	Calculation	132 ± 2	[g]
m_6	Lower shaft	Calculation	Calculation	3.8 ± 0.2	[g]
m_7	Dowel pin	Mcmaster	Calculation	2.7 ± 0.2	[g]
$m_{8,1}$	Bearing inner race	SP601 balance	Manufacturer spec.	2.9 ± 0.1	[g]
$m_{8,2}$	Bearing ball spacer	SP601 balance	Manufacturer spec.	0.2 ± 0.1	[g]
$m_{8,3}$	Bearing ball	SP601 balance	Manufacturer spec.	0.3 ± 0.1	[g]
$m_{8,4}$	Bearing outer race	SP601 balance	Manufacturer spec.	6.5 ± 0.1	[g]
m_9	Lower arm	Calculation	Calculation	116 ± 2	[g]
m_{10}	Upper tracker	SP601 balance	Calculation	0.2 ± 0.1	[g]
m_{11}	Lower tracker	SP601 balance	Calculation	0.3 ± 0.1	[g]
m_{12}	Upper arm tape	SP601 balance	Calculation	0.7 ± 0.1	[g]
m_{13}	Lower arm tape	SP601 balance	Calculation	0.6 ± 0.1	[g]
\bar{r}_4	Top pivot to set screw	Calculation	Calculation	4.0 ± 0.5	[mm]
ℓ_u	Top to bottom pivot	Calipers & calculation	Calculated	171.9 ± 0.3	[mm]
\bar{r}_5	Top pivot to bar 1.	Calipers & calculation	Calculated	86.0 ± 0.2	[mm]
\bar{r}_9	Bottom pivot to bar 2 ref.	Calipers & calculation	Calculated	71.5 ± 0.4	[mm]
\bar{I}_1	Encoder inertia	Manufacturer spec.	Manufacturer spec.	2000 ± 200	[g · mm ²]
\bar{I}_2	Flex couple inertia	Solidworks	Calculated	1100 ± 5	[g · mm ²]
$\bar{I}_{3,1}$	Inner race inertia	Solidworks	Uncertainty negligible	103	[g · mm ²]
$\bar{I}_{3,2}$	Ball spacer inertia	Calculated	Uncertainty negligible	40 ± 20	[g · mm ²]
$\bar{I}_{3,3}$	Bearing ball inertia	Solidworks	Uncertainty negligible	0.4	[g · mm ²]
\bar{I}_4	Upper shaft inertia	Calculated	Uncertainty negligible	242 ± 4	[g · mm ²]
\bar{I}_5	Upper arm inertia	Calculated	Calculated	470000 ± 9000	[g · mm ²]
\bar{I}_6	Lower shaft inertia	Calculated	Calculated	12 ± 1	[g · mm ²]
\bar{I}_7	Dowel pin inertia	Calculated	Calculated	61 ± 2	[g · mm ²]
$\bar{I}_{8,1}$	Inner race inertia	Solidworks	Uncertainty negligible	103	[g · mm ²]
$\bar{I}_{8,2}$	Ball spacer inertia	Calculated	Uncertainty negligible	2.5	[g · mm ²]
$\bar{I}_{8,3}$	Bearing ball inertia	Solidworks	Uncertainty negligible	0.4	[g · mm ²]
$\bar{I}_{8,4}$	Outer race inertia	Solidworks	Uncertainty negligible	544	[g · mm ²]
\bar{I}_9	Bottom bar inertia	Calculated	Calculated	245000 ± 5000	[g · mm ²]
\bar{I}_{10}	Upper tracker	Solidworks	Calculation	4 ± 1	[g · mm ²]
\bar{I}_{11}	Lower tracker	Solidworks	Calculation	9 ± 1	[g · mm ²]
\bar{I}_{12}	Upper arm tape	Solidworks	Calculation	2500 ± 200	[g · mm ²]
\bar{I}_{13}	Lower arm tape	Solidworks	Calculation	1300 ± 200	[g · mm ²]
d_I	Inner race diameter	Calipers	Calculation	11.062 ± 0.002	[mm]
d_B	Bearing ball diameter	Calipers	Calculation	3.932 ± 0.002	[mm]

Table 9: Variable substitutions for energy equations pertaining to Configuration A

Variable	Definition
ψ	$\frac{1}{2} \left\{ \bar{I}_1 + \bar{I}_2 + \bar{I}_{3,1} D_{11}^2 + 2m_{3,3} (D_{11} \frac{d_I+d_B}{2})^2 + 2\bar{I}_3 2D_{11}^2 + 2\bar{I}_{3,3} C_{11}^2 + 2\bar{I}_4 + 2m_4 \bar{r}_4^2 + 2\bar{I}_5 + 2m_5 \bar{r}_5^2 + 2\bar{I}_6 + 2m_6 \ell_u^2 + \bar{I}_7 + m_7 \ell_u^2 + 2\bar{I}_{8,1} + 2m_{8,1} \ell_u^2 + 2\bar{I}_{8,2} D_{11}^2 + 2m_{8,2} \ell_u^2 + 14m_{8,3} \left[\ell_u^2 + (D_{11} \frac{d_I+d_B}{2})^2 \right] + 14\bar{I}_{8,3} C_{11}^2 + m_{8,4} \ell_u^2 + m_9 \ell_u^2 + \bar{I}_{10} \right\}$
λ	$\frac{1}{2} \left\{ 2(\bar{I}_{8,2} D_{22}^2 + 7m_{8,3} (D_{12} \frac{d_I+d_B}{2})^2) + \bar{I}_{8,4} \right\} + m_9 \bar{r}_9 + \bar{I}_9$
ζ	$\frac{1}{2} \left\{ 2(\bar{I}_{8,2} + 7m_{8,3} D_{11} D_{12} (\frac{d_I+d_B}{2})^2) - \bar{I}_{8,3} C_{11} C_{12} \right\}$
σ	$g \left\{ 2m_4 \bar{r}_4 + 2m_5 \bar{r}_5 + \ell_u (2m_6 + m_7 + 2(m_{8,1} + m_{8,2} + 7m_{8,3} + m_{8,4} + m_{8,5})) + m_9 \ell_u \right\}$
κ	$g \left\{ m_9 \bar{r}_9 \right\}$
C_{11}	$\frac{d_I}{2d_B}$
C_{12}	$\frac{d_I+2d_B}{2d_B}$
D_{11}	$\frac{d_I}{2(d_I+2B)}$
D_{12}	$\frac{d_I+d_B}{2(d_I+d_B)}$
A_1	$2\frac{7}{2}m_{8,3}\ell_u D_{11}(d_I + d_B)$
A_2	$2\frac{7}{2}m_{73}\ell_u D_{12}(d_I + d_B)$
$A_3,$	$m_9 \bar{r}_9 \ell_u$

A.6 Mechanical Drawings

The following mechanical drawings are provided for the sake of reproduction. The encoder flange, encoder mount, and side trackers are best produced via additive manufacturing. The lower and upper links are best produced by machining stock aluminum.

